PCCP

Accepted Manuscript

ROYAL SOCIETY OF CHEMISTRY

www.rsc.org/pccp

Artificially Maturated [FeFe] Hydrogenase from C*hlamydomonas reinhardtii*: A HYSCORE and ENDOR Study of a Non-Natural H-cluster

Agnieszka Adamska-Venkatesh[1], Trevor R. Simmons[2], Judith F. Siebel[1], Vincent Artero[2], Marc Fontecave[2,3], Edward Reijerse[1], Wolfgang Lubitz[1]

[1] Max Planck Institut für Chemische Energiekonversion, Stiftstrasse 34-36, 45470 Mülheim an der Ruhr, Germany

[2] Laboratoire de Chimie et Biologie des Métaux; Université Grenoble Alpes , CEA, CNRS, 17 rue des martyrs, 38000 Grenoble, France

[3] Laboratoire de Chimie des Processus Biologiques, Collège de France, Université Pierre et Marie Curie, CNRS UMR 8229, 11 place Marcelin Berthelot, 75005 Paris, France

I. Abstract

Hydrogenases are enzymes that catalyze the oxidation of H_2 as well as the reduction of protons to form H_2. The active site of [FeFe] hydrogenase is referred to as the “H-cluster” and consists of a “classical” [4Fe-4S] cluster connected *via* a bridging cysteine thiol group to a unique $[2Fe]_H$ sub-cluster, containing CN^- and CO ligands as well as a bidentate azadithiolate ligand. It has been recently shown that the biomimetic $[Fe_2(adt)(CO)_4(CN)_2]^{2-}$ (adt^{2-} = azadithiolate) complex resembling the diiron sub-cluster can be inserted *in vitro* into the apo-protein of [FeFe] hydrogenase, which contains only the [4Fe-4S] part of the H-cluster, resulting in a fully active enzyme. This synthetic tool allows convenient incorporation of a variety of diiron mimics, thus generating hydrogenases with artificial active sites. [FeFe] hydrogenase from *Chlamydomonas reinhardtii* maturated with the biomimetic complex $[Fe_2(pdt)(CO)_4(CN)_2]^{2-}$ (pdt^{2-} = propanedithiolate), in which the bridging adt^{2-} ligand is replaced by pdt^{2-}, can be stabilized in a state strongly resembling the active oxidized (H_{ox}) state of the native protein. This state is EPR active and the signal originates from the mixed valence Fe^IFe^{II} state of the diiron sub-cluster. Taking advantage of the variant with ^{15}N and ^{13}C isotope labeled CN^- ligands we performed HYSCORE and ENDOR studies on this hybrid protein. The ^{13}C hyperfine couplings originating from both CN^- ligands were determined and assigned. Only the ^{15}N coupling from the CN^- ligand bound to the

terminal iron was observed. Detailed orientation selective ENDOR and HYSCORE experiments at multiple field positions enabled the extraction of accurate data for the relative orientations of the nitrogen and carbon hyperfine tensors. These data are consistent with the crystal structure assuming a g-tensor orientation following the local symmetry of the binuclear sub-cluster.

II. Introduction

Over the last few decades, the growing interest in renewable energy technologies has stimulated research on biotechnological hydrogen production using microorganisms[1-9]. A wide range of microorganisms from archaea, bacteria to some eukaryotes use metalloenzymes called hydrogenases as a part of their energy metabolism[1,10]. Hydrogenases catalyze the reversible conversion of molecular hydrogen into two protons and two electrons. The hydrogenases can be classified into three groups, according to the metal composition of their active site: [NiFe] hydrogenases with the subgroup of [NiFeSe] hydrogenases, [FeFe] hydrogenases and [Fe] hydrogenases[9,10]. The [FeFe] hydrogenases were found to be the most active for hydrogen production *in vivo*[11,12]. The quite unique active site of these enzymes is highly conserved, and referred to as the "H-cluster"[9,13-16]. It contains a typical $[4Fe\text{-}4S]_H$ cluster, which is coupled by one of its coordinating cysteine side groups to a unique binuclear sub-cluster $[2Fe]_H$ shown in figure 1[9,13-16]. The low oxidation states of the iron atoms in the binuclear sub-cluster are stabilized by CN^- and CO ligands[13,17]. In addition, a bidentate dithiol ligand bridges the two iron centers. For many years the nature of the central atom of this ligand was strongly debated, since it could not be uniquely identified in the crystal structure[13,14,16,18]. However, soon after the crystal structures became available, based on structural and mechanistic arguments an amine function was proposed[13]. This proposal was later experimentally supported by pulsed EPR data[19,20]. In recent studies it was shown that it is possible to insert various biomimetic complexes into the unmaturated [FeFe] hydrogenase that contains only the $[4Fe\text{-}4S]_H$ part of the H-cluster[21,22]. It was shown that the enzyme was fully activated only when the biomimic complex $[Fe_2(adt)(CO)_4(CN)_2]^{2-}$ (adt^{2-} = azadithiolate) containing the amine group in the dithiolate bridging ligand (adt^{2-}) was inserted, whereas those activated with complexes containing other dithiolate ligands showed very little or no activity[21-23]. Spectroscopic characterization of this “hybrid” enzyme showed it to be indistinguishable from the native one[24].

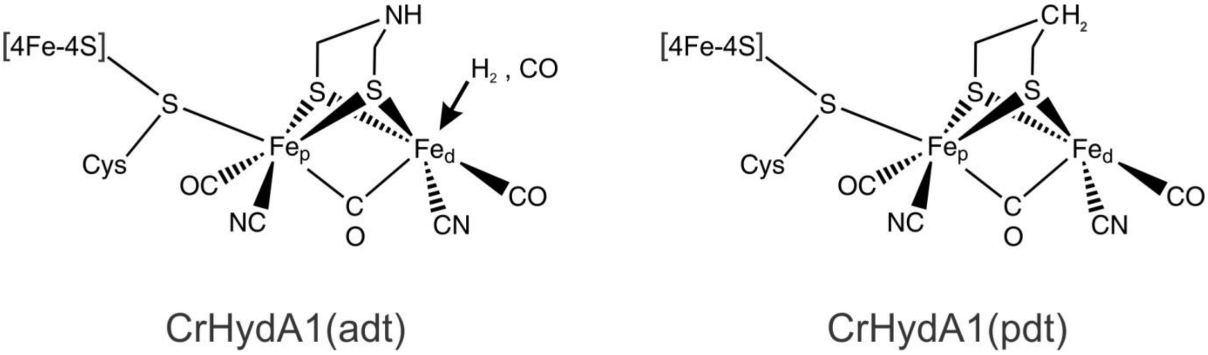

Figure 1. Schematic representation of the structure of the H-cluster of artificially maturated [FeFe] hydrogenase from *C. reinhardtii* with natural CrHydA1(adt) and the non-natural CrHydA1(pdt) binuclear sub-site.

The H-cluster of the isolated native enzyme usually exists as a mixture of redox states that have been identified and spectroscopically characterized[9]. The oxidized active state H_{ox} is characterized by a mixed valence configuration of the $[2Fe]_H$ sub-cluster (Fe^IFe^{II}), while the $[4Fe\text{-}4S]_H$ sub-cluster is in the oxidized 2+ state ($2Fe^{II}2Fe^{III}$)[9,17,25]. The iron atoms in the $[2Fe]_H$ sub-cluster are in a low spin state and exhibit a characteristic rhombic S=1/2 EPR signal[9,25]. This state can be inhibited by external CO, generating the H_{ox}-CO state, which is electronically very similar to H_{ox} but shows an axial EPR signal[9]. This signal is often present in [FeFe] hydrogenase preparations due to the so-called “cannibalization process” in which the CO ligands from light or oxygen damaged H-clusters are released and captured by H-clusters that are still intact[24,26-28].

In the algal [FeFe] hydrogenase from *Chlamydomonas reinhardtii* (CrHydA1), upon two fully reversible one electron reductions, H_{ox} is converted first to the active reduced state H_{red} and then to the “super reduced” active state H_{sred}[28]. It was recently shown that the H_{ox}-CO state can also be reversibly reduced to the CO inhibited reduced state $H_{'red'}$-CO, which, upon subsequent reversible one electron reduction (accompanied with CO dissociation), yields the H_{sred} state[24]. This state is paramagnetic and gives a signal characteristic for a reduced $[4Fe\text{-}4S]^+$ cluster, while both iron atoms in the $[2Fe]_H$ sub-cluster are antiferromagnetically coupled in an Fe^IFe^I (S = 0) configuration[29].

The electronic structure of H_{ox} and H_{ox}-CO have previously been the subject of intensive investigation[9,19,25-28,30-35]. The ^{57}Fe hyperfine interactions indicate that the spin density distribution over the H-cluster drastically changes upon conversion from H_{ox} to H_{ox}-CO[25]. In the H_{ox} state, the unpaired spin density is more or less equally distributed over both iron atoms in the $[2Fe]_H$ sub-cluster, while in the H_{ox}-CO state most of spin density is shifted towards the proximal iron. The formally diamagnetic $[4Fe\text{-}4S]_H^{2+}$ sub-cluster has a strong influence on the electronic structure of the binuclear sub-cluster because in model complexes in which the cubane sub-cluster is lacking, the spin distribution clearly deviates from what is found in the native system[25,32,36-38]. By studying ^{13}C labeled CO ligands and signals from ^{14}N in the CN^- ligands it was found that in the H_{ox}-CO state the spin density is largely distributed over the CO ligands, while almost no spin density was detected on the CN^- ligands[33]. A different situation was observed in the H_{ox} state. ^{14}N ESEEM studies showed a very rich pattern of hyperfine couplings that was assigned to the nitrogen from the CN^- ligand bound to the distal iron, the nitrogen in the dithiolate bridge and the nitrogen of the side chain of the lysine hydrogen bonded to the distal CN^- ligand[39,19]. No spin density was found for the CN^- ligand bound to the proximal iron.

In a recent study it was shown that CrHydA1 maturated with the biomimic complex $[Fe_2(pdt)(CO)_4(CN)_2]^{2-}$ (pdt^{2-} = propanedithiolate) (referred as pdt complex) containing a CH_2 group in the dithiolate bridge affords an almost inactive hybrid enzyme CrHydA1(pdt) that can be stabilized in two redox states (oxidized and reduced)[23,24]. FTIR and EPR studies showed that the oxidized form of CrHydA1(pdt) is almost identical to the native H_{ox} state[40]. It is therefore concluded that the $[2Fe]_H$ sub-cluster (Fe^IFe^{II}) is in the mixed valence configuration, while the $[4Fe\text{-}4S]_H$ sub-cluster is oxidized (2+). It was suggested that reduction takes place in the $[4Fe\text{-}4S]_H$ sub-cluster and due to strong exchange coupling within the H-cluster this state is EPR silent. No other states (including H_{ox}-CO) were observed for this hybrid.

In the present study, we confirm through detailed EPR studies that oxidized CrHydA1(pdt) can be used as a good structural and electronic model system for the native H_{ox} state. As discussed below the pdt analog offers multiple advantages: (i) straightforward synthesis and stability of the pdt complex; (ii) the possibility to obtain a pure redox state for the reconstituted enzyme, thus facilitating spectroscopic characterization. To obtain additional information about the spin density distribution over the CN^- ligands we synthesized ^{13}C and ^{15}N labeled pdt complex and performed HYSCORE and ENDOR experiments on the labeled H-cluster of the reconstituted hydrogenase.

III. Materials and methods

Sample preparation

All chemicals used were purchased from Sigma-Aldrich and used as received unless otherwise stated. Solvents were freshly distilled under an inert atmosphere of argon from an appropriate drying agent. FTIR spectra of synthetic complexes were recorded on a Perkin Elmer Spectrum-100 spectrometer *via* a thin film solution. $Fe_2(pdt)(CO)_6$ and $[Et_4N]_2[Fe_2(pdt)(CO)_4(CN)_2]$ were prepared according to literature procedures[41,42], while $[Et_4N]_2[Fe_2(pdt)(CO)_4(^{13}CN)_2]$ and $[Et_4N]_2[Fe_2(pdt)(CO)_4(C^{15}N)_2]$ were prepared by modified literature procedures as described below.

$[Et_4N]_2[Fe_2(pdt)(CO)_4(^{13}CN)_2]$

$Fe_2(pdt)(CO)_6$ (0.15 g, 0.40 mmol) was dissolved in MeCN (10 ml) and added *via* a cannula to a solution of $[K][^{13}CN]$ (0.05 g, 0.80 mmol) in MeOH (5 ml) under argon. The reaction mixture was stirred for 2 hours at room temperature to give a dark red solution. $[Et_4N][Br]$ (0.20 g, 0.95 mmol) dissolved in MeCN (10 ml) was added to the reaction mixture, which was allowed to stir for an additional hour. The solvent was removed under reduced pressure to give a dark red solid. This was dissolved in acetone (10 ml) and filtered *via* a cannula to give a dark red filtrate. The solution was mixed with EtOAc (20 ml) and cooled to -26 °C to give $[Et_4N]_2[Fe_2(pdt)(CO)_4(^{13}CN)_2]$ as a deep red crystalline solid (0.18 g, 72%) ν_{max}/cm^{-1} (acetonitrile) 2032 (^{13}CN), 1963, 1922, 1885, 1871 (sh) (CO).

$[Et_4N]_2[Fe_2(pdt)(CO)_4(C^{15}N)_2]$

$Fe_2(pdt)(CO)_6$ (0.07 g, 0.20 mmol) was dissolved in MeCN (5 ml) and added *via* a cannula to a solution of $[K][C^{15}N]$ (0.03 g, 0.40 mmol) in MeOH (2 ml) under argon. The reaction mixture was stirred for 2 hours at room temperature to give a dark red solution. $[Et_4N][Br]$ (0.10 g, 0.50 mmol) dissolved in MeCN (5 ml) was added to the reaction mixture, which was allowed to stir for an additional hour. The solvent was removed under reduced pressure to give a dark red solid. This was dissolved in acetone (5 ml) and filtered *via* a cannula to give a dark red filtrate. The solution was mixed with EtOAc (10 ml) and cooled to -26 °C to give $[Et_4N]_2[Fe_2(pdt)(CO)_4(C^{15}N)_2]$ as a deep red crystalline solid (0.08 g, 65%) ν_{max}/cm^{-1} (acetonitrile) 2046 ($C^{15}N$), 1963, 1922, 1884, 1871 (sh) (CO).

Enzyme maturation

Unmaturated CrHydA1 containing only the [4Fe-4S] cluster was expressed and isolated from *Escherichia coli* as described earlier[22,43]. Active [FeFe] hydrogenase was obtained through direct insertion of the binuclear sub-site complex as described previously[22,23]. CrHydA1(pdt) was prepared in 25 mM Tris/HCl, pH 8.0, 25 mM KCl. Samples were oxidized by stepwise titration with thionine monitored by FTIR. All manipulations and treatments were done under strict anaerobic conditions.

FTIR measurements

Fourier transform infrared (FTIR) measurements on the artificially maturated proteins were carried out using a Bruker IFS 66v/s FTIR spectrometer equipped with a nitrogen cooled Bruker mercury cadmium telluride (MCT) detector. The spectra were accumulated in the double-sided, forward-backward mode with 1000 scans (14 minutes) and a resolution of 2 cm^{-1} at 15 °C. Data processing was facilitated by home written routines in the MATLAB™ programming environment.

EPR measurements

Field swept X- and Q-band EPR spectra were recorded in the pulsed mode using FID detection after a 1μs π/2 excitation pulse. After a pseudomodulation transformation, the spectra obtained in this way are comparable to those using CW EPR[44].

Electron nuclear double resonance (ENDOR) was used to study the ^{13}C hyperfine interactions. In this investigation the Davies ENDOR sequence was used: $[\pi]$-t_{d1}-[RF]-t_{d2}-$[\pi/2]$-τ-$[\pi]$-τ-(ESE)[45,46]. The excitation of nuclear spin transitions is detectable through an increase in the inverted ESE intensity. The microwave preparation pulse was set to 140 ns, whereas the length of the radiofrequency (RF) pulse was adjusted through an RF nutation experiment in order to maximize the ENDOR effect.

Hyperfine sublevel correlation spectroscopy (HYSCORE) experiments were performed to extract the ^{15}N and ^{14}N hyperfine interactions using the standard HYSCORE pulse sequence: $[\pi/2]$-τ-$[\pi/2]$-t_1-$[\pi]$-t_2-$[\pi/2]$-τ-(ESE)[46-48]. The length of the microwave $[\pi/2]$ and $[\pi]$ pulses was adjusted to the maximum available microwave power (1kW). The delay between the first two pulses (τ) was adjusted in order to avoid “blind spots” in the important spectral regions using a series of three pulse ESEEM experiments as a function of

τ. The starting t_1 and t_2 delays in all measurements were 100 ns. To suppress the effect of unwanted echoes, a four step phase cycling of the microwave pulses was used.

X-band measurements were performed on a Bruker ELEXYS E-580 X-band spectrometer with a SuperX-FT microwave bridge and a Bruker ER EN4118X-MD4 ENDOR dielectric resonator. Cryogenic temperatures (10-20 K) were obtained by an Oxford CF935 flow cryostat. ENDOR experiments were performed using the random (stochastic) acquisition technique and making use of a 500W ENI 5100 L RF amplifier.

Q-band experiments were performed on a Bruker ELEXYS E580 spectrometer with a SuperQ-FT microwave bridge and a home built resonator described earlier[49]. Cryogenic temperatures (10-20 K) were obtained by an Oxford CF935 flow cryostat. ENDOR experiments were performed using the random (stochastic) acquisition technique and making use of a 300W ENI 300 L RF amplifier. A Trilithic^{TM} H4LE35-3-AA-R high-power low pass filter (cut off frequency around 35 MHz) was used to suppress the "harmonics" of the ^{1}H ENDOR signals.

Data analysis and simulation

The simulations of the EPR, ENDOR and HYSCORE spectra were based on the spin Hamiltonian approach

$$H_0 = \beta_e \vec{\boldsymbol{B}}_{\boldsymbol{0}} \cdot \boldsymbol{g} \cdot \vec{\boldsymbol{S}} - \sum_i g_{n,i}\beta_n \vec{\boldsymbol{B}}_{\boldsymbol{0}} \cdot \vec{\boldsymbol{I}}_{\boldsymbol{i}} + \sum_{\boldsymbol{i}} \vec{\boldsymbol{S}} \cdot \boldsymbol{A}_{\boldsymbol{i}} \cdot \vec{\boldsymbol{I}}_{\boldsymbol{i}} + \sum_{\boldsymbol{i}} \vec{\boldsymbol{I}}_{\boldsymbol{i}} \cdot \boldsymbol{P}_{\boldsymbol{i}} \cdot \vec{\boldsymbol{I}}_{\boldsymbol{i}}$$

where β_e is the Bohr magneton, β_n the nuclear magneton, $g_{n,i}$ the g-factor of the ith nucleus and $\boldsymbol{g}$ represents the electronic g-tensor, $\vec{\boldsymbol{B}}_{\boldsymbol{0}}$ the magnetic field vector, $\vec{\boldsymbol{S}}$ the effective spin vector, $\vec{\boldsymbol{I}}_{\boldsymbol{i}}$ nuclear spin vector, $\boldsymbol{A}_{\boldsymbol{i}}$ the hyperfine tensor, $\boldsymbol{P}_{\boldsymbol{i}}$ the nuclear quadrupole tensor and the sum runs over all nuclei (i) interacting with the unpaired electron spin. The first and the second terms represent the electron and nuclear Zeeman effects. The third term represents the hyperfine interaction of the unpaired electron with the nuclear spins and the last term represents the quadrupole coupling. The last term was used in the simulations only for ^{14}N nuclei where I=1. The quadrupole tensor $\boldsymbol{P}_{\boldsymbol{i}}$ is traceless and its principal values can be rewritten in the following way:

$$\left[P_x, P_y, P_z\right] = \frac{e^2qQ}{4I(2I-1)h}\left[-(1-\eta), -(1+\eta), 2\right] \ .$$

In this work we will use the two parameters: $K = \frac{e^2qQ}{4I(2I-1)h}$ and $\eta = \frac{P_x - P_y}{P_z}$ with $|P_z| \geq |P_y| \geq |P_x|$ and $0 \leq \eta \leq 1$ to characterize the quadrupole coupling.

All the simulations were performed in the EasySpin based program written in the MATLAB^{TM} environment[50]. ENDOR spectra were simulated using the “salt” routine and the frequency domain calculations of HYSCORE spectra were simulated using the “saffron” routine. Signals corresponding to the different nuclei were simulated separately in order to reduce computing time.

The orientations of the hyperfine and quadrupole tensors are presented with respect to the principal axes of the electronic g-tensor using Euler angles. In the convention used in EasySpin the first rotation is by angle α along the z axis, the second by angle β around the new y’ axis and the third by angle γ around the new z’’ axis[46]. The geometric details e.g. distances and angles for the [2Fe] sub-cluster used for the g-tensor orientation within the H-cluster molecular structure were extracted from the X-ray crystal data using the Pymol software[51].

IV. Results

FTIR of reduced and oxidized CrHydA1(pdt)

Figure 2 shows the FTIR spectra obtained for CrHydA1 with inserted labeled and non-labeled $[Fe_2(pdt)(CO)_4(CN)_2]^{2-}$ complexes in the reduced (“as obtained”) and thionine oxidized states. Each spectrum contains only one component indicating that the preparations represent pure states and do not contain residual unbound $[Fe_2(pdt)(CO)_4(CN)_2]^{2-}$ complexes in solution. The IR band positions in the spectra obtained for non-labeled CrHydA1(pdt) are in agreement with previously reported data[21,22,24]. Upon labeling the CN^- ligands of the pdt complexes the IR bands originating from the CO ligands are not affected while the ones originating from CN^- vibrations are shifted by 29-31 cm^{-1} upon ^{15}N exchange and 43-46 cm^{-1} upon ^{13}C exchange.

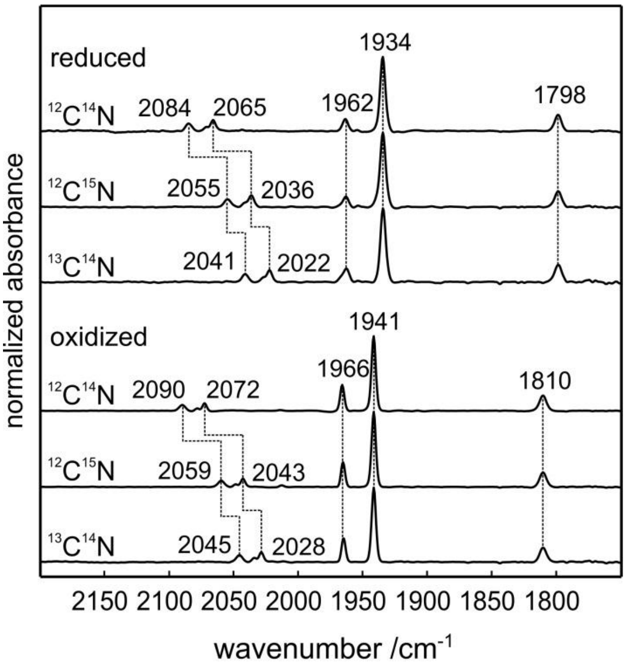

Figure 2. Normalized FTIR spectra recorded for CrHydA1(pdt) containing non-labeled and two labeled pdt complexes in the reduced and oxidized states measured at 15°C. In the labeled complexes either N or C was labeled. All samples were prepared in 25 mM Tris/HCl, pH 8.0, 25 mM KCl. Oxidized samples also contained thionine.

The EPR spectrum obtained for oxidized non-labeled CrHydA1(pdt) shows a pure state characterized by a rhombic signal virtually identical to the one obtained for native H_{ox} (see supplementary information). The obtained g-values 2.093, 2.038 and 1.996, are in agreement with previously reported data on CrHydA1(pdt)[24].

It has been shown previously using ^{57}Fe ENDOR that for the native H-cluster in the H_{ox} state the spin density is delocalized over both iron atoms in the binuclear sub-cluster[25]. Additional information about the electronic structure can be obtained by investigating the distribution of the unpaired spin density over the ligands of the binuclear sub-cluster. In particular, the CN^- ligands are of great interest and previously controlled isotope labeling of these ligands was not easily obtained[52,53].

^{13}C interaction of the CN^- ligands

The effect of ^{13}C labeling of the CN^- ligands is readily evident in the X-band EPR spectra where a splitting of all three g-components is easily observed (see figure 3A). In the Q-band EPR spectra this ^{13}C hyperfine splitting is, however, washed out due to the increased line broadening. The X-band EPR spectra already allow an estimation of the ^{13}C hyperfine coupling with principal values in the range of 21-29 MHz (depending on the g position) suggesting one strongly coupled ^{13}C. More accurate values of this coupling can be obtained using ENDOR spectroscopy. Moreover, this technique also allows for the identification of much weaker couplings that are not resolved in the EPR of ^{13}CN labeled CrHydA1(pdt).

The most prominent signal in the X-band Davies ENDOR spectra (see figure 3B) recorded at the three canonical positions is centered at 14.5 MHz and is also present in the non-enriched sample (see supplementary information). This ^{1}H ENDOR signal with maximum splitting of 3.5 MHz is very similar to the one obtained for native H_{ox} and was assigned to the β-protons of the cysteine ligands coordinating the $[4Fe\text{-}4S]_H$ sub-cluster[37]. At this point, a full analysis of this signal is not possible due to the overlap of contributions from at least eight different protons. The observation of this ^{1}H signal, however, confirms that the electronic structure of H_{ox} in CrHydA1(pdt) is virtually identical to that of native H_{ox} in which part of the spin density is delocalized on the $[4Fe\text{-}4S]_H$ sub-cluster.

In the X-band Davies ENDOR spectra (see figure 3B) two additional signals around and partially overlapping with the ^{1}H ENDOR signal are observed, which are split by twice the Larmor frequency of ^{13}C. The position of these signals at half the hyperfine interaction of the strongly coupled carbon nucleus is consistent with the splitting observed in the X-band pseudomodulated FID detected EPR spectrum (see figure 3A). However, it is not possible to simulate the spectra with high accuracy due to the large linewidth of these signals and their partial overlap with the ^{1}H ENDOR signals. At low frequency the ENDOR spectra in figure 3B show another very sharp line around 6 MHz. This signal can be assigned to the weakly coupled ^{13}C of the second CN^- ligand. The low frequency line belonging to this doublet will fall below 1.5 MHz and cannot be detected due to the low sensitivity of the Davies ENDOR method in this frequency range.

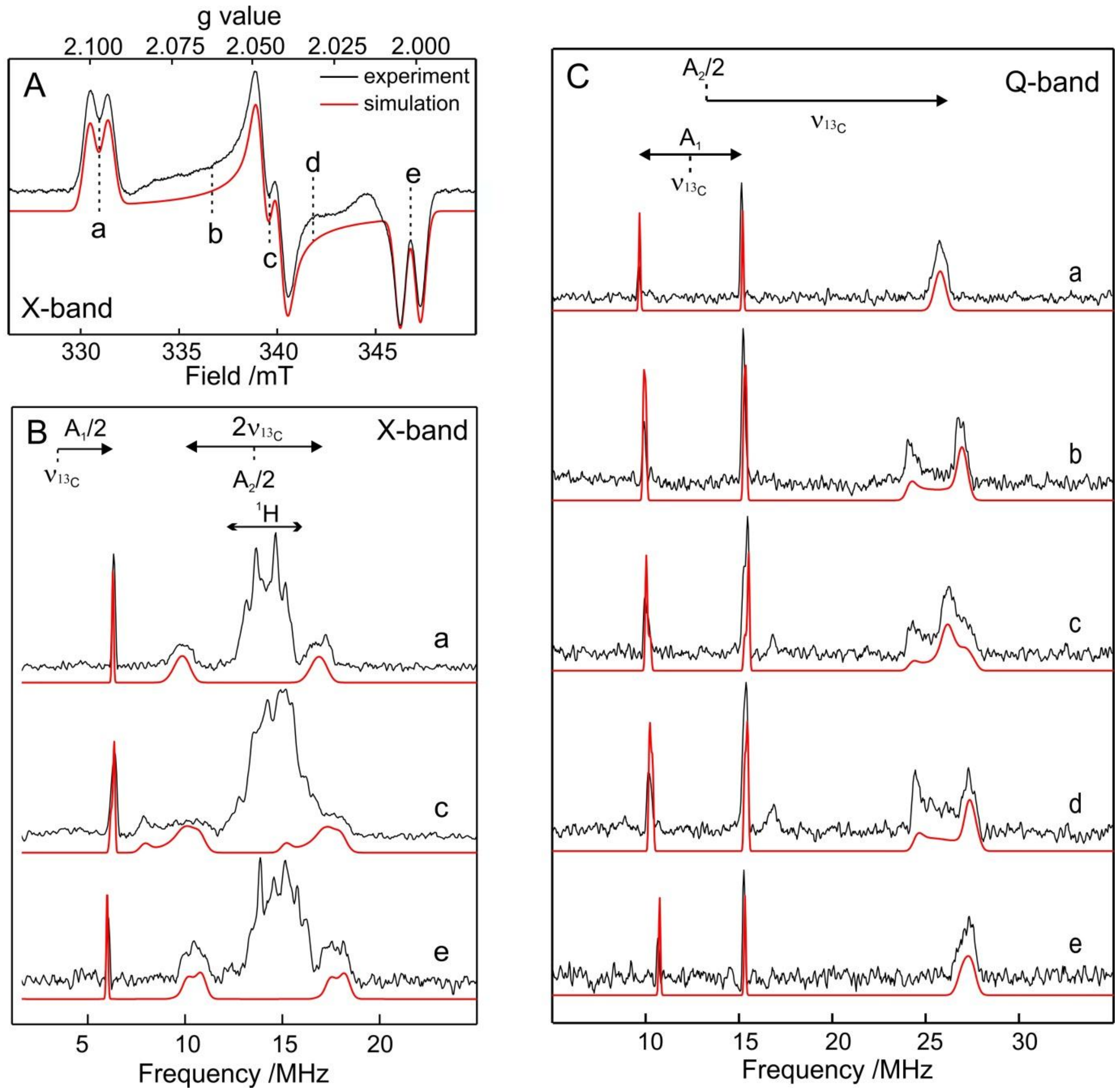

Figure 3. EPR and ENDOR spectra recorded for oxidized CrHydA1(pdt) with ^{13}C labeled CN$^-$ ligands at 15 K including simulations. A) First derivative of X-band FID detected EPR spectra, microwave pulse length 1 μs, shot repetition time 2 ns, microwave frequency 9.715 GHz. The field positions at which the ENDOR spectra were recorded are marked a) to e). B) X-band Davies ENDOR spectra recorded with an RF pulse of 20 μs, shot repetition time 2 μs, microwave frequency 9.716 GHz, field positions: a) 330.9 mT (g_1), c) 339.7 mT (g_2), e) 346.8 mT (g_3). C) Q-band Davies ENDOR spectra recorded with an RF pulse of 20 μs, shot repetition time 2 μs, microwave frequency 33.921 GHz, field positions: a) 1158.2 mT (g_1), b) 1176.65 mT c) 1189.3 mT (g_2), d) 1195.1 mT e) 1213.6 mT (g_3). The black line represents experimental data and the red line the sum of the simulations. The assignment of the hyperfine splittings is indicated above the figure. The X-band FID detected EPR and Davies ENDOR spectra were simulated using the hyperfine values determined from the Q-band Davies ENDOR spectra.

Complementary information can be obtained from the Q-band Davies ENDOR spectra, which were measured at five field positions and are presented in figure 3C. Here, only the high frequency transition of the ^{13}C doublet assigned to the strongly coupled cyanide ligand is visible and now appears around 27 MHz. Due to the better orientation selection and higher sensitivity at Q-band, the spectral resolution is enhanced as compared to the X-band ENDOR spectra. Both ENDOR signals assigned to the weakly coupled ^{13}C are observable and can be simulated very accurately. Table 1 shows all obtained parameters, which were also used to simulate the spectra presented in figure 3.

Table 1. Principal values of the ^{13}C hyperfine tensor of the CN$^-$ ligands of the oxidized CrHydA1(pdt).

	A_1 (MHz)	A_2 (MHz)	A_3 (MHz)	A_{iso} (MHz)	α (°)	β (°)	γ (°)
A_{1C}	5.52 (0.05)	5.52 (0.05)	4.55 (0.05)	5.2	0 (10)	0 (10)	0 (10)
A_{2C}	30 (0.5)	28.5 (0.5)	22.7 (0.5)	27.1	0 (10)	119 (10)	46 (10)

The signs of the hyperfine couplings cannot be determined. Numbers in parenthesis are uncertainties.

Both hyperfine tensors have an axial or nearly axial character but A_{2C}(iso) is around five times larger than A_{1C}(iso), which indicates a substantial difference in the spin density distribution over the two CN$^-$ ligands. By virtue of the well resolved ^{13}C-ENDOR lineshapes for the strongly coupled A_{2C} (see figure 3C), the relative orientation of A_{2C} with respect to the g-tensor could be determined with high precision (table 1). The Euler angles of the hyperfine interaction tensor A_{2C} in the g-tensor axis frame are remarkably similar to the orientation of the Fe-CN bond relative to the Fe-Fe vector extracted from the X-ray crystal structures of CpI and DdH (see figure 4). As discussed below, assuming A_{2C} is oriented along the Fe-CN bond, this information can be used to make proposals concerning the g-tensor orientation within the H-cluster.

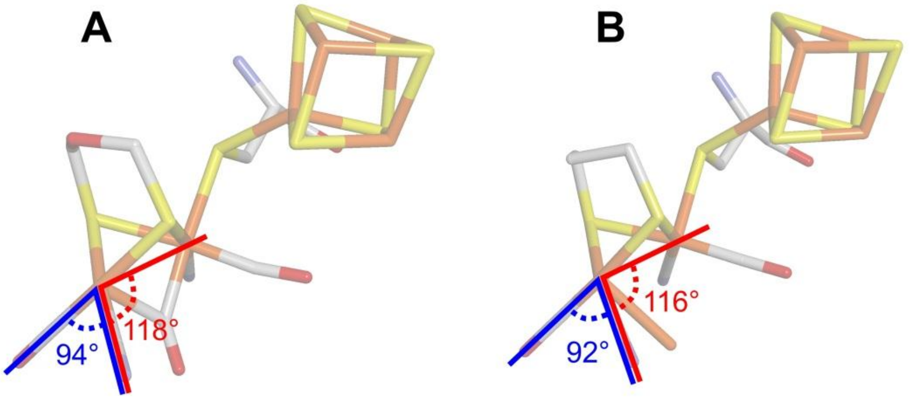

Figure 4. The H-cluster according to the X-ray structures obtained for CpI (A) and DdH (B) with marked angles between the Fe-Fe vector and the Fe-C(N) bond (red) and between the Fe-C(N) and Fe-C(O) bonds (blue)[14,18].

^{15}N interaction of the CN$^-$ ligands

The ^{14}N hyperfine couplings were previously obtained for DdH in the H_{ox} state and can be used to compare the oxidized CrHydA1(pdt) system to the native one[19]. The obtained

HYSCORE spectra of DdH in the H_{ox} state were very crowded due to the contributions of three ^{14}N nuclei with different quadrupole interactions. In the DdH study, these three ^{14}N signals were assigned to the distal CN^-, the adt amine group and the coordinating Lys amine[19]. The ^{15}N labeled CrHydA1(pdt) hybrid protein offers a substantial simplification with respect to the CrHydA1(adt). Since the bridging amine is lacking and both CN^- ligands are enriched with ^{15}N, HYSCORE spectra are much easier to interpret.

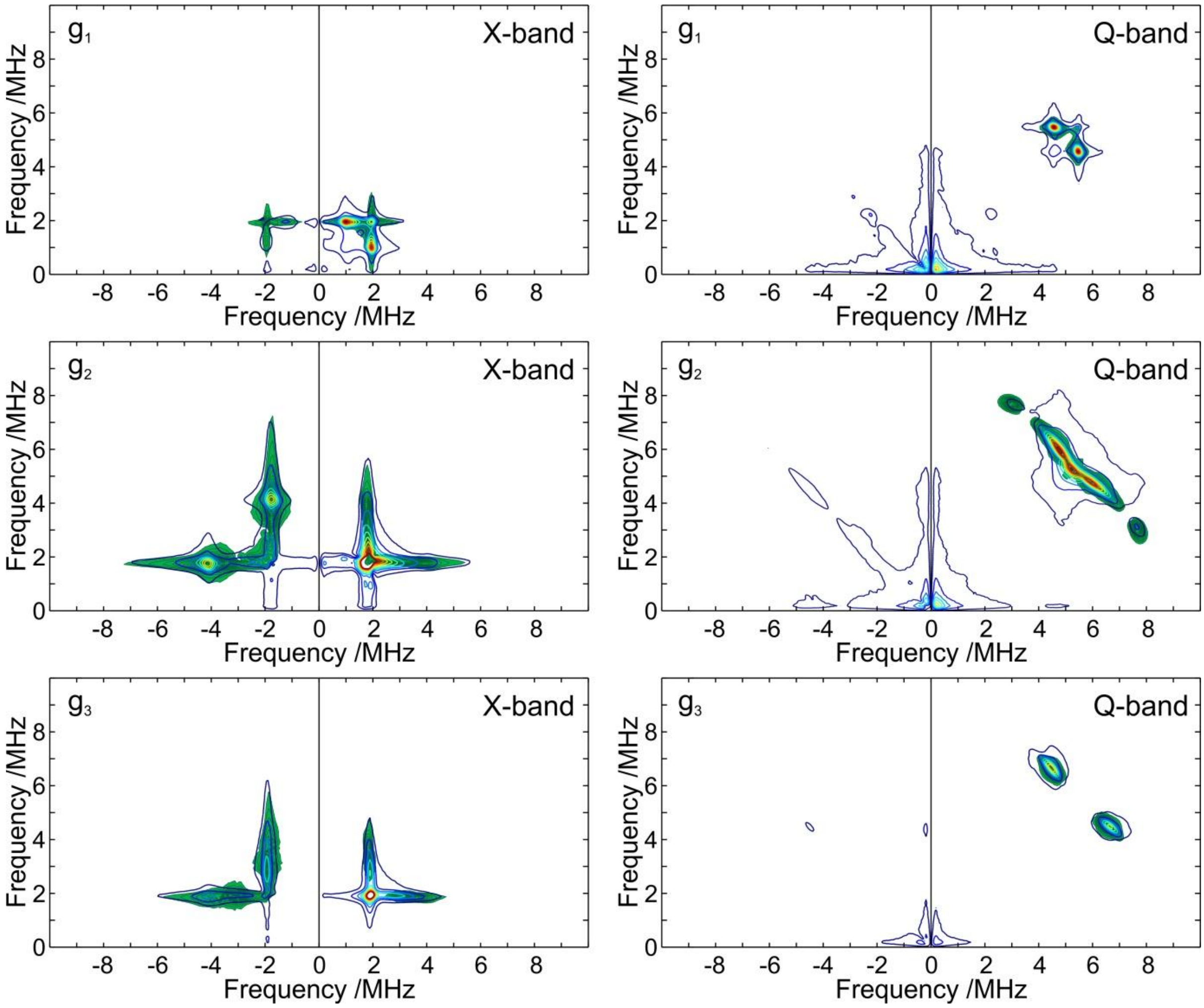

Figure 5. X-band and Q-band HYSCORE spectra recorded for oxidized CrHydA1(pdt) with ^{15}N labeled CN^- ligands at 20 K. Simulations are indicated in color (green). Left: X-band HYSCORE spectra recorded with t_1 and t_2 step 16 ns, shot repetition time 500 μs, microwave frequency 9.709 GHz, delay between two first microwave pulses (τ) 180 ns, length of microwave pulses (π/2) 8 ns and field positions (from the top) (g_1) 330.6 mT, (g_2) 339.5 mT, (g_3) 346.5 mT. Right: Q-band HYSCORE spectra recorded with t_1 and t_2 step 16 ns, shot repetition time 500 μs, microwave frequency 33.879 GHz, delay between two first microwave pulses (τ) 268 ns, length of microwave pulses (π/2) 16 ns and field positions (from the top) (g_1) 1156.9 mT, (g_2) 1187.7 mT, (g_3) 1212.5 mT. All the spectra were simulated using parameters from table 2 and are presented in green overlaid with the experimental results.

Figure 5 shows the CrHydA1(pdt)-$C^{15}N$ orientation selective HYSCORE spectra at X and Q-band overlaid with their simulations. The hyperfine simulation parameters are presented in table 2. In general, in the HYSCORE spectra cross-peaks originating from nuclei with weak hyperfine couplings ($|\nu_n|>|A/2|$) appear in the (++) quadrant, and spectral features associated with strong hyperfine couplings ($|\nu_n|<|A/2|$) show up in the (-+) quadrant. While X-band HYSCORE signals occur in both (++) and (-+) quadrants of the 2D pattern, the Q-band HYSCORE spectra show only contributions in the (++) quadrant. This already allows the conclusion that the ^{15}N hyperfine principal values are in the range of twice the Larmor frequency at X-band (i.e. around 1.5 MHz)[46].

Table 2. Principal values of the ^{15}N hyperfine tensor of the CN^- ligands of the oxidized CrHydA1(pdt).

A_1 (MHz)	A_2 (MHz)	A_3 (MHz)	A_{iso} (MHz)	α (°)	β (°)	γ (°)
-1.3 (0.2)	-1.1 (0.2)	6.2 (0.2)	1.3	0 (10)	50 (10)	90 (10)

The signs of the hyperfine couplings cannot be determined. Numbers in parenthesis are uncertainties.

Although both CN^- ligands are labeled with ^{15}N only one ^{15}N contribution is observed in the HYSCORE spectra. It is reasonable to assign this nitrogen to the CN^- ligand in which we observed the strongly coupled ^{13}C. Assuming that the isotropic hyperfine interaction of ^{13}C in a CN^- ligand is a reflection of the spin density at that ligand, the spin density ratio between the two CN^- ligands is larger by a factor of 5. If the same ratio would apply to the nitrogen nuclei of the CN^- ligands the corresponding ^{15}N coupling of the “weakly coupled” ligand is expected to be ≈0.25 MHz and this would be too small to be detectable.

The hyperfine tensor obtained for ^{15}N also has a nearly axial character. Interestingly, the orientation of the hyperfine tensor obtained for ^{15}N is different from the one obtained for the strongly coupled ^{13}C. The X-ray crystal structure indicates that both nitrogen atoms create hydrogen bonds with surrounding amino acids. The nitrogen in the CN^- ligand bound to the distal iron atom can create three hydrogen bonds. It is shown in figure 6 that the distances and angles between this CN^- ligand and the hydrogen bonds formed with Lys, Pro, Gln or Ile (for CpI and DdH, respectively) are very similar in both structures. The related angles are in the range from 99° to 139°. Evaluation of the relative angles between the ^{15}N and ^{13}C hyperfine tensors (see supplementary information) would suggest that the z axis of the ^{15}N hyperfine tensor should be aligned along one of the hydrogen bonds, or at least is strongly affected by the presence of multiple hydrogen bonds in which the CN^- nitrogen takes part.

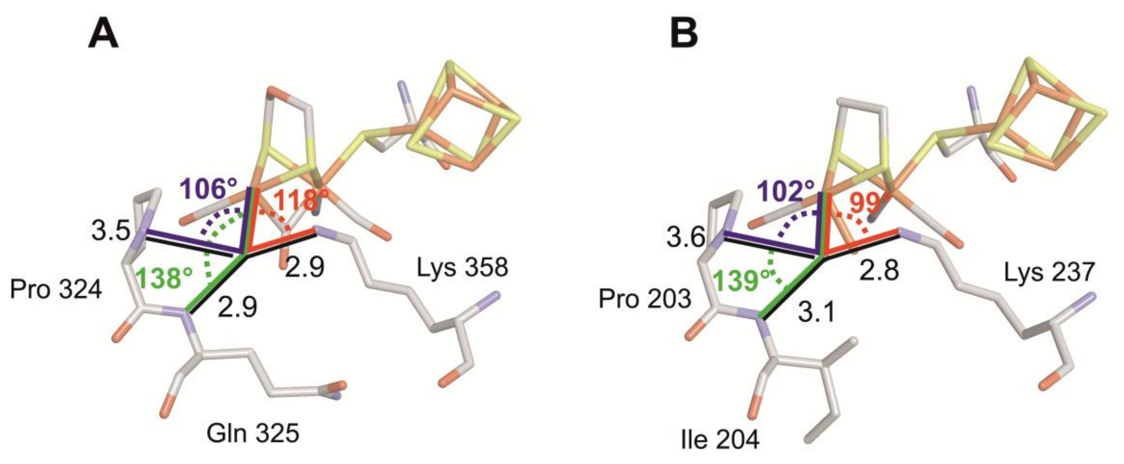

Figure 6. The H-cluster from the X-ray structures obtained for CpI (A) and DdH (B) with marked angles between the CN^- ligand and the H-bond donor in lysine (red), proline (violet) and glutamine or isoleucine (green), respectively[14,18]. In black are marked distances in Å between nitrogen atoms.

^{14}N Hyperfine and quadrupole coupling of the CN^- ligand

The ^{15}N hyperfine interactions of the distal CN^- ligand determined in the previous section can now be used to assess the signals from the naturally abundant ^{14}N CN^- signals of CrHydA1(pdt). X- and Q-band field dependent HYSCORE spectra measured at g_1 and g_2 for DdH [FeFe] hydrogenase in the H_{ox} state have been previously reported[19], therefore to allow for the direct comparison of the results for oxidized CrHydA1(pdt) with native H_{ox} DdH studies with identical experimental settings were used. The obtained spectra are hardly distinguishable from the previously published data (see supplementary information). This demonstrates that after incorporation into the apo-protein of [FeFe] hydrogenase the modified pdt complex is “assembled” in the same way as the native H-cluster. Moreover the active site in [FeFe] hydrogenases from algae and bacteria are virtually identical.

For the sample containing native [FeFe] hydrogenases prepared in the H_{ox} state it is very common that EPR spectra contain an additional component originating from the H_{ox}-CO state. The additional signal rather strongly overlaps with the high field part of the H_{ox} spectrum, especially with the g_3 position, and significantly hinders or precludes assignment of the signal components in the HYSCORE spectra measured at this field. For oxidized CrHydA1(pdt) we can take advantage of the fact that no additional, overlapping signals are present. The ^{14}N HYSCORE spectrum measured at the field position corresponding to g_3 shows a very rich, informative pattern. The obtained X-band and Q-band HYSCORE spectra together with their simulation are presented in figure 7.

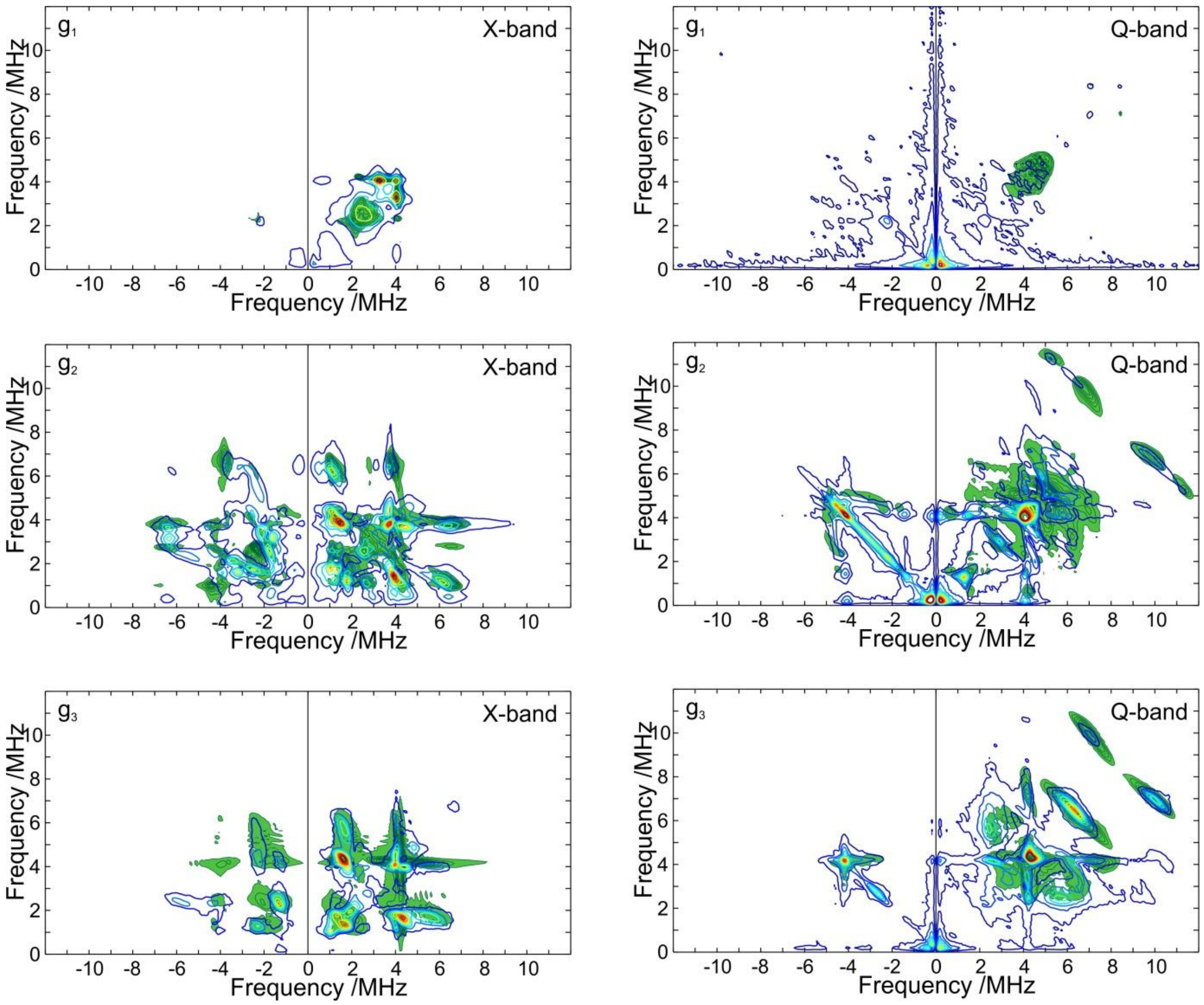

Figure 7. X-band and Q-band HYSCORE spectra measured for oxidized CrHydA1(pdt) at 20 K. Simulations are indicated in color (green). Left: X-band HYSCORE spectra recorded with t_1 and t_2 step 16 ns, shot repetition time 500 μs, microwave frequency 9.717 GHz, delay between two first microwave pulses (τ) 180 ns, length of microwave pulses (π/2) 8 ns and field positions (from the top) (g_1) 330.8 mT, (g_2) 339.9 mT, (g_3) 346.9 mT. Right: Q-band HYSCORE spectra recorded with t_1 and t_2 step 16 ns, shot repetition time 500 μs, microwave frequency 33.867 GHz, delay between two first microwave pulses (τ) 268 ns, length of microwave pulses (π/2) 16 ns and field positions (from the top) (g_2) 1187.4 mT, (g_3) 1212.1 mT. All the spectra were simulated using parameters from table 3 and are presented in green and overlaid with the experimental results.

The ^{14}N HYSCORE features are dominated by the nuclear quadrupole interaction, which strongly depends on the ligand surrounding. For the ^{14}N from CN$^-$ the quadrupole parameter K lies in the range between 0.7 and 1.0 MHz. The ^{14}N hyperfine parameters are much more difficult to extract from the HYSCORE spectra. Therefore, we used the scaled hyperfine values obtained from the ^{15}N HYSCORE experiments (table 2) and included previously reported quadrupole parameters as starting values in our simulations, only changing the orientation of the quadrupole tensor. The resulting simulation parameters are presented in table 3 and the corresponding spectra are overlaid with the experimental data as shown in figure 7. Both single and double quantum HYSCORE features are represented very well by the simulations. The obtained quadrupole parameters K and η are in agreement with previously obtained values for the CN^- ligands in DdH as well as an inorganic $[2Fe]_H$ model complex[19,54]. The ^{14}N nuclear quadrupole interaction Euler angles, however, deviate from the previously estimated value for DdH in H_{ox}. This could be due to inaccuracies in the determination of the Euler angles for DdH, which had to be extracted from three overlapping ^{14}N HYSCORE patterns[19]. Interestingly, the CN^- ^{14}N quadrupole tensor seems to be aligned with the ^{13}C hyperfine tensor (table 1 and 3). This would support the assumption that the z-axes of both the ^{14}N quadrupole and ^{13}C hyperfine tensors are aligned along the Fe-CN_d bond (see below).

Table 3. Principal values of the ^{14}N hyperfine and quadrupole tensors of the oxidized CrHydA1(pdt) and previously assigned to CN_d in H_{ox} DdH and in a model complex[19,54].

Hyperfine coupling

A_1 (MHz)	A_2 (MHz)	A_3 (MHz)	A_{iso} (MHz)	α (°)	β (°)	γ (°)	
-0.9 (0.2)	-0.8 (0.2)	4.4 (0.2)	0.9	0 (10)	50 (10)	90 (10)	pdt
1.5 (0.4)	3.8 (0.2)	-0.4 (0.2)	1.5	41 (10)	24 (10)	0 (10)	H_{ox} DdH[19]
0.86	3.00	1.04	1.63	-	-	-	model[54]

Quadrupole coupling

K (MHz)	η	α (°)	β (°)	γ (°)	
0.9 (0.03)	0.34 (0.02)	0 (10)	119 (10)	46 (10)	pdt
0.95 (0.03)	0.34 (0.02)	-26 (10)	24 (10)	0 (10)	H_{ox} DdH[19]
0.91	0.00	-	-	-	model[54]

The signs of the hyperfine couplings have not been determined. Numbers in parenthesis are uncertainties.

V. Discussion

Spin density distribution

It was found previously that in the native H_{ox} state of the H-cluster the spin density is distributed over both iron atoms in the $[2Fe]_H$ sub-cluster[25]. Our current results on the oxidized CrHydA1(pdt) show that the modified active site in this hybrid protein basically shows the same electronic structure. The ENDOR signal from the weakly coupled β-protons of the cysteines that coordinate the $[4Fe\text{-}4S]_H$ sub-cluster is identical for CrHydA1(pdt) and DdH (native) (figure S5 in supplementary information) suggesting that the same inter-cluster exchange interaction occurs in both proteins.

In recent work by Myers et al.[53], the [FeFe] hydrogenase from *C. pasteurianum* was generated *in vitro* using the maturases HydE, HydF and HydG in combination with ^{13}C and ^{15}N labeled tyrosine as substrate for HydG. Analogous to our current work, the CN^- ligands of the H-cluster were isotopically labeled with ^{13}C and ^{15}N, and the signals from two CN^- ^{13}C nuclei and one from ^{15}N were observed. The same large difference in the spin density distribution over both carbons was found (≈5:1) and the signal from the nitrogen was assigned to the CN^- ligand in which we observed the strongly coupled ^{13}C[53]. The ^{14}N HYSCORE spectra obtained for oxidized CrHydA1(pdt) strongly resembles previously reported spectra for native H_{ox} in DdH[19]. In this work, supported by DFT calculations of the ^{14}N quadrupole interactions, the ^{14}N signal was assigned to the CN^- ligand bound to the distal iron atom[19]. The ^{57}Fe hyperfine couplings indicated an almost equal spin distribution between the two irons in the bi-nuclear sub-cluster[25]. In contrast, the couplings observed for the two CN^- ligands are very different. Apparently the electronic structure is strongly affected by the different coordination geometry of the two iron atoms and the inter-cluster exchange interaction between the $[2Fe]_H$ and $[4Fe\text{-}4S]_H$ clusters. This causes the hyperfine couplings of the two CN^- ligands to be different.

Due to the absence of the adt^{2-} bridging amine in oxidized CrHydA1(pdt), the ^{14}N HYSCORE spectra are substantially simplified as compared to the situation for the native H_{ox} state in DdH, where three ^{14}N signals are observed (CN^-, adt, and Lys)[19]. Since the surrounding of the H-cluster is highly conserved one would expect to observe the same Lys ^{14}N contributions as in the native DdH H_{ox} state. However, in the spectra obtained for the protein labeled with $[Fe_2(pdt)(CO)_4(C^{15}N)_2]^{2-}$ no signals originating from natural abundance ^{14}N(Lys) were present. The HYSCORE spectra obtained for non-labeled oxidized CrHydA1(pdt) could be simulated with parameters describing only one component. The reported hyperfine coupling for the lysine in DdH is very small (A_{iso} = 0.57 MHz)[19]. It is possible that this signal is overlapping with signals originating from the CN^- ligand, but this is rather unlikely. Since there may be small differences in structure between the algal hydrogenase used in this study and the bacterial DdH enzyme used in the work of Silakov et al.[19], one can also speculate that less spin density is delocalized towards the Lys in CrHydA1 and the ^{14}N(Lys) hyperfine coupling can, therefore, no longer be observed.

Orientation of the g tensor within the H-cluster

Unfortunately, up to now, DFT studies on the H-cluster were not successful in predicting the magnetic resonance properties of the iron core (g-tensor and ^{57}Fe hyperfine interaction) with any confidence[55,56]. Although the effect of CO binding to the exchangeable site (i.e. a spin density shift towards the $[4Fe\text{-}4S]_H$ sub-cluster) is correctly predicted, the influence of the [4Fe-4S] cluster is not represented very well. In fact, the DFT predicted spin density distributions rather reflect the situation occurring in binuclear model complexes without the $[4Fe\text{-}4S]_H$ unit[32,37,38,56]. In H_{ox}-CO, a strong inter-cluster exchange (95 cm^{-1}) interaction is apparent, based on the ^{57}Fe hyperfine interaction data, which led us to speculate that the g_z-component could be oriented along the inter-cluster axis[25]. Since in H_{ox} and oxidized CrHydA1(pdt) the inter-cluster exchange interaction is much smaller (25 cm^{-1}) and the spin density seems to be equally distributed over both iron atoms in $[2Fe]_H$, it is reasonable to assume that the vector connecting Fe_p and Fe_d represents a local symmetry axis and defines the orientation of the g tensor[25]. The other g-axis would be defined by the local symmetry plane through both irons and the bridging CO ligand (bisecting the dithiol ligand). Figure 8 shows the proposed g-tensor axis orientation and the angles of the Fe_d-CN bond in this axis system. The Euler angles of both the CN^- carbon hyperfine A_{2C} and nitrogen quadrupole Q_N tensors, (0,119,46) degrees, correspond to a rotation matrix, which defines the orientation of the tensor z-components with respect to the g-tensor axes as (127, 51, 119) degrees. These values fit perfectly to the orientation of the Fe-CN bond with respect to the g-tensor orientation as proposed in figure 8.

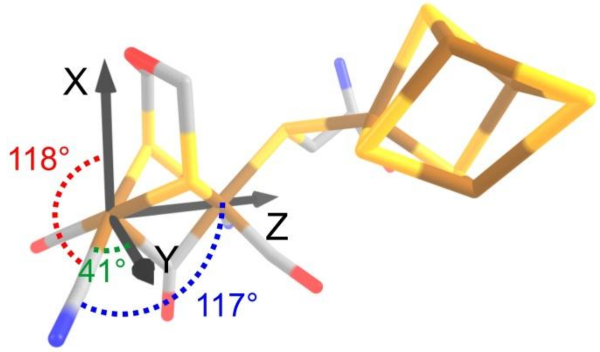

Figure 8. The coordinate system describing the position of the g-tensor overlaid onto the H-cluster from the X-ray structure obtained for CpI[18].

VI. Conclusions

The oxidized state of the artificially maturated CrHydA1(pdt) hybrid is shown to be a very accurate and useful structural mimic of the native active oxidized state of CrHydA1. The ^{1}H ENDOR and ^{14}N HYSCORE spectra of oxidized CrHydA1(pdt) are virtually indistinguishable from those of native H_{ox} (apart from the lacking ^{14}N adt^{2-} contribution). The high resolution ^{15}N and ^{13}C hyperfine interaction data of the CN^{-} ligands confirmed the previously proposed model of the electronic structure of the H-cluster in which the spin density is delocalized over the two iron atoms of the bi-nuclear sub-cluster. In addition, the accurate data on the relative orientation of the distal CN^{-} ligand in the g-axis frame, allowed the suggestion of an orientation of the g-tensor adapted to the local symmetry of the complete binuclear sub-cluster in which the Fe-Fe bond represents one of the g- principal axes. The accurate data obtained on the $^{14}N/^{15}N$ coupling of the distal CN^{-} ligand will facilitate the assignment and analysis of the nitrogen couplings of the adt bridge in the CrHydA1(^{15}N adt) hybrid, which is currently under investigation in our group. Although oxidized CrHydA1(pdt) is shown to be a perfect structural and electronic mimic for native $H_{ox,}$ even showing residual hydrogenase activity, the other resting states of the native enzyme (H_{red}, H_{sred} and H_{ox}-CO) are lacking[23,24]. At this point it is not clear how this intriguing behavior can be related to the presence or absence of the bridging amine (adt) function. Detailed comparative spectroscopic and quantum chemical investigations may reveal the subtle structural dependencies triggering the conversion between the diverging resting (and intermediate) states of CrHydA1(pdt) and CrHydA1(adt). The current study is one of the first steps in this endeavor.

VII. Acknowledgements

We would like to thank Gudrun Klihm for her excellent technical support in the EPR experiments. Furthermore, the Max Planck Society, the Deutsche Forschungsgemeinschaft (DIP project), the Life Science Division of CEA (Bio-energy program), the French National Research Agency (NiFe–Cat project, ANR–10–BLAN–711, Labex program ARCANE, ANR-11-LABX-0003-01 and DYNAMO, ANR-11-LABX-0011) and from Fondation de l’Orangerie for individual Philanthropy and its donors are gratefully acknowledged for their financial support. The authors are grateful to Dr. James Birrell for critically reading the manuscript and his useful suggestions on content and language.

VIII. Notes and references

(1) *Hydrogen as a Fuel: Learning from Nature*, Cammack, R.; Frey, M.; Robson, R., eds.; Talor & Francis: London **2001**.

(2) Nath, K.; Das, D. *Appl. Microbiol. Biotechnol.* **2004**, *65*, 520.

(3) Kotay, S. M.; Das, D. *Int. J.Hydrogen Energy* **2008**, *33*, 258.

(4) Miyake, J.; Igarashi, Y.; Rögner, M. *Biohydrogen III*, **2004**.

(5) Rand, D. A. J.; Dell, R. M. *Hydrogen Energy Challenges and Prospects*, RSC Publishing: Cambridge, **2008**.

(6) Mertens, R.; Liese, A. *Curr. Opin. Biotechnol.* **2004**, *15*, 343.

(7) Kim, J. Y. H.; Cha, H. J. *Korean J. Chem. Eng.* **2013**, *30*, 1.

(8) Bockris, J. O. M. *Int. J.Hydrogen Energy* **2013**, *38*, 2579.

(9) Lubitz, W.; Ogata, H.; Rüdiger, O.; Reijerse, E. *Chem. Rev.* **2014**, *114*, 4081.

(10) Vignais, P. M.; Billoud, B. *Chem. Rev.* **2007**, *107*, 4206.

(11) Stripp, S. T.; Happe, T. *Dalton Trans.* **2009**, *45*, 9960.

(12) Hatchikian, E. C.; Forget, N.; Fernandez, V. M.; Williams, R.; Cammack, R. *Eur. J. Biochem.* **1992**, *209*, 357.

(13) Nicolet, Y.; de Lacey, A. L.; Vernede, X.; Fernandez, V. M.; Hatchikian, E. C.; Fontecilla-Camps, J. C. *J. Am. Chem. Soc.* **2001**, *123*, 1596.

(14) Nicolet, Y.; Piras, C.; Legrand, P.; Hatchikian, C. E.; Fontecilla-Camps, J. C. *Struct. Fold. Des.* **1999**, *7*, 13.

(15) Lemon, B. J.; Peters, J. W. *Biochemistry* **1999**, *38*, 12969.

(16) Peters, J. W.; Lanzilotta, W. N.; Lemon, B. J.; Seefeldt, L. C. *Science* **1998**, *282*, 1853.

(17) Pierik, A. J.; Hulstein, M.; Hagen, W. R.; Albracht, S. P. J. *Eur. J.Biochem.* **1998**, *258*, 572.

(18) Pandey, A. S.; Harris, T. V.; Giles, L. J.; Peters, J. W.; Szilagyi, R. K. *J. Am. Chem. Soc.* **2008**, *130*, 4533.

(19) Silakov, A.; Wenk, B.; Reijerse, E.; Lubitz, W. *Phys.Chem.Chem. Phys.***2009**, *11*, 6592.

(20) Erdem, Ö. F.; Schwartz, L.; Stein, M.; Silakov, A.; Kaur-Ghumaan, S.; Huang, P.; Ott, S.; Reijerse, E. J.; Lubitz, W. *Angew.Chem., Int.Ed.* **2011**, *50*, 1439.

(21) Berggren, G.; Adamska, A.; Lambertz, C.; Simmons, T.; Esselborn, J.; Atta, M.; Gambarelli, S.; Mouesca, J.; Reijerse, E.; Lubitz, W.; Happe, T.; Artero, V.; Fontecave, M. *Nature* **2013**, *499*, 66.

(22) Esselborn, J.; Lambertz, C.; Adamska-Venkatesh, A.; Simmons, T.; Berggren, G.; Noth, J.; Siebel, J.; Hemschemeier, A.; Artero, V.; Reijerse, E.; Fontecave, M.; Lubitz, W.; Happe, T. *Nat. Chem. Biol.* **2013**, *9*, 607.

(23) Siebel, J.F.; Adamska-Venkatesh, A.; Weber, K.; Rumpel, S.; Reijerse, E.; Lubitz, W. *Biochemistry* **submitted for publication**.

(24) Adamska-Venkatesh, A.; Krawietz, D.; Siebel, J.; Weber, K.; Happe, T.; Reijerse, E.; Lubitz, W. *J. Am. Chem. Soc.* **2014**, *136*, 11339.

(25) Silakov, A.; Reijerse, E. J.; Albracht, S. P. J.; Hatchikian, E. C.; Lubitz, W. *J. Am. Chem. Soc.* **2007**, *129*, 11447.

(26) Albracht, S. P. J.; Roseboom, W.; Hatchikian, E. C. *J. Biol. Inorg. Chem.***2006**, *11*, 88.

(27) Roseboom, W.; de Lacey, A. L.; Fernandez, V. M.; Hatchikian, E. C.; Albracht, S. P. J. *J. Biol. Inorg. Chem.* **2006**, *11*, 102.

(28) Silakov, A.; Kamp, C.; Reijerse, E.; Happe, T.; Lubitz, W. *Biochemistry* **2009**, *48*, 7780.

(29) Adamska, A.; Silakov, A.; Lambertz, C.; Rüdiger, O.; Happe, T.; Reijerse, E.; Lubitz, W. *Angew.Chem., Int.Ed.* **2012**, *51*, 11458.

(30) Lubitz, W.; Reijerse, E.; van Gastel, M. *Chem. Rev.* **2007**, *107*, 4331.

(31) Chen, Z. J.; Lemon, B. J.; Huang, S.; Swartz, D. J.; Peters, J. W.; Bagley, K. A. *Biochemistry* **2002**, *41*, 2036.

(32) Silakov, A.; Olsen, M. T.; Sproules, S.; Reijerse, E. J.; Rauchfuss, T. B.; Lubitz, W. *Inorg.Chem.***2012**, *51*, 8617.

(33) Silakov, A.; Wenk, B.; Reijerse, E.; Albracht, S. P. J.; Lubitz, W. *J. Biol. Inorg. Chem.* **2009**, *14*, 301.

(34) Pereira, A. S.; Tavares, P.; Moura, I.; Moura, J. J. G.; Huynh, B. H. *J. Am. Chem. Soc.* **2001**, *123*, 2771.

(35) Pierik, A. J.; Hagen, W. R.; Redeker, J. S.; Wolbert, R. B. G.; Boersma, M.; Verhagen, M.; Grande, H. J.; Veeger, C.; Mutsaers, P. H. A.; Sands, R. H.; Dunham, W. R. *Eur. J. Biochem.* **1992**, *209*, 63.

(36) Popescu, C. V.; Münck, E. *J. Am. Chem. Soc.* **1999**, *121*, 7877.

(37) Silakov, A.; Reijerse, E. J.; Lubitz, W. *Eur. J. Inorg. Chem.* **2011**, *7*, 1056.

(38) Silakov, A.; Shaw, J. L.; Reijerse, E. J.; Lubitz, W. *J. Am. Chem. Soc.* **2010**, *132*, 17578.

(39) Van Dam, P. J.; Reijerse, E. J.; Hagen, W. R. *Eur. J. Biochem.***1997**, *248*, 355.

(40) Preliminary Mössbauer and ^{57}Fe ENDOR measurements (not shown) confirm this finding.

(41) Seyferth, D.; Womack, G. B.; Gallagher, M. K.; Cowie, M.; Hames, B. W.; Fackler, J. P.; Mazany, A. M. *Organometallics* **1987**, *6*, 283.

(42) Le Cloirec, A.; Best, S. P.; Borg, S.; Davies, S. C.; Evans, D. J.; Hughes, D. L.; Pickett, C. J. *Chem. Commun.* **1999**, 2285.

(43) Kuchenreuther, J. M.; Grady-Smith, C. S.; Bingham, A. S.; George, S. J.; Cramer, S. P.; Swartz, J. R. *PLoS One* **2010**, *5*, e15491.

(44) Hyde, J. S.; Pasenkiewicz-Gierula, M.; Lesmanowicz, A.; Antholine, W. E. *Appl. Magn. Reson.* **1990**, *1*, 483.

(45) Davies, E. R. *Phys. Lett. A* **1974**, *A 47*, 1.

(46) Schweiger, A.; Jeschke, G. *Principles of Pulse Electron Paramagnetic Resonance*; Oxford University Press : Oxford, **2001**.

(47) Höfer, P.; Grupp, A.; Nebenführ, H.; Mehring, M. *Chem. Phys. Lett.* **1986**, *132*, 279.

(48) Shane, J. J.; Hofer, P.; Reijerse, E. J.; Deboer, E. *J. Magn. Reson.* **1992**, *99*, 596.

(49) Reijerse, E.; Lendzian, F.; Isaacson, R.; Lubitz, W. *J. Magn. Reson.* **2012**, *214*, 237.

(50) Stoll, S.; Schweiger, A. *J. Magn. Reson.* **2006**, *178*, 42.

(51) The PyMOL Molecular Graphics System. Version 1.5.0.4 Schrödinger, LLC.

(52) Kuchenreuther, J. M.; George, S. J.; Grady-Smith, C. S.; Cramer, S. P.; Swartz, J. R. *PLoS One* **2011**, *6*, e20346.

(53) Myers, W. K.; Stich, T. A.; Suess, D. L. M.; Kuchenreuther, J. M.; Swartz, J. R.; Britt, R. D. *J. Am. Chem. Soc.* **2014**, *136*, 12237.

(54) Erdem, Ö. F.; Stein, M.; Kaur-Ghumaan, S.; Reijerse, E. J.; Ott, S.; Lubitz, W. *Chem.Eur. J.* **2013**, *19*, 14566.

(55) Fiedler, A. T.; Brunold, T. C. *Inorg.Chem.* **2005**, *44*, 9322.

(56) Greco, C.; Silakov, A.; Bruschi, M.; Ryde, U.; De Gioia, L.; Lubitz, W. *Eur. J. Inorg. Chem.* **2011**, *7*, 1043.